Comput Mech (2009) 44:651–668
DOI 10.1007/s00466-009-0398-z

ORIGINAL PAPER

Insight into a model for large strain anisotropic elasto-plasticity

Do-Nyun Kim · Francisco Javier Montáns · Klaus-Jürgen Bathe

Received: 2 January 2009 / Accepted: 7 May 2009 / Published online: 3 June 2009

Abstract Efficient and accurate simulation of the deformations in anisotropic metallic sheets requires a constitutive model and an accompanying algorithm at large strains which take into account the anisotropy of both the elastic and plastic material behaviors, as well as their evolution with plastic strains. Recently we proposed such a constitutive model based on continuum energy considerations, the Lee decomposition and an anisotropic stored energy function of the logarithmic strains in which the rotation of the orthotropic axes is also considered. We obtained a framework similar to the one used in isotropic elasto-plasticity. In the present work we give some physical insight into the parameters of the model and their effects on the predictions, both in proportional and in non-proportional loading problems. We also present a procedure to obtain the spin parameter of the model from Lankford R-values.

Keywords Plasticity · Anisotropic plasticity · Orthotropy · Plastic spin · Large strain plasticity

1 Introduction

Accurate modeling of the elasto-plastic deformations of metals is very important not only for the simulation of the manufacturing process but also for the analysis of the final components during their service, for example consider the simulation of car crash or crush conditions. Many metallic goods are made from cold-rolled sheets. Rolling, as well as many other manufacturing procedures, induces anisotropy in the metals. Anisotropy manifests itself in that the physical properties depend on the directions along which they are measured. Hence the constants determining the elastic and plastic properties, notably the Young's moduli and yield stresses become dependent on the direction of testing. An accurate computational model must take into account the directions of both the elastic and plastic properties, as well as their evolution with plastic strains.

Most computational simulations are currently using continuum models and finite element procedures, see for example [1,2]. Since the 1990s simulations of isotropic elasto-plasticity at large strains have achieved reasonable accuracy and efficiency [3], using combined isotropic-kinematic hardening [4] and consistently linearized implicit implementations [5,6]. The principal ingredients of the most successful elasto-plastic implementations at large strains are the use of the multiplicative or Lee decomposition [7], hyperelasticity in terms of the logarithmic strains and the exponential function to integrate the plastic gradient [5,8]. The multiplicative decomposition is based on micromechanical observations and uses the existence of an intermediate, local, configuration uniquely determined from the evolution of the local plastic flow (both plastic strain and plastic rotation tensors) [9]. An advantage of the use of the Lee decomposition is that, since the elastic stretch tensor is explicitly obtained, the total elastic strains may be directly computed from the deformation gradient. Then, the use of a stored energy function gives stresses without resorting to 'rate' expressions [10–13], thus avoiding any algorithmic objectivity issue and dissipation during purely elastic strain paths [14,15].

D.-N. Kim · K. J. Bathe (✉)
Department of Mechanical Engineering,
Massachusetts Institute of Technology,
Cambridge, MA 02139, USA
e-mail: kjb@mit.edu

D.-N. Kim
e-mail: kingddo@mit.edu

F. J. Montáns
Departamento de Vehículos Aeroespaciales,
Universidad Politécnica de Madrid, Madrid, Spain
e-mail: fco.montans@upm.es

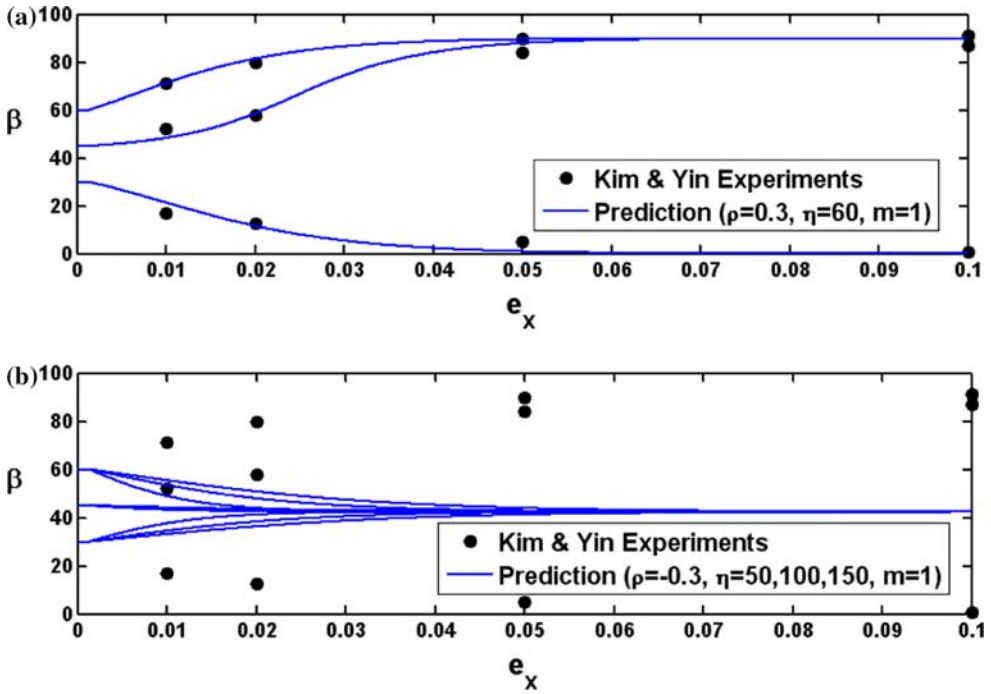

Fig. 1 The evolution of the principal orthotropic directions at different spatial strains e_x when uniaxial tensile loading is applied to a metal sheet along the x-axis. β is the angle between the rolling direction and the loading direction (x-axis). Three initial orientations (30°, 45° and 60°) of orthotropic axis are considered. See [9,32] for the detailed description of the experiment and the analysis. The other material parameters are listed in Table 1

However, the Lee decomposition presents important computational issues due to its multiplicative character, inserting the Mandel stress tensor in the dissipation expression [6,9]. The resulting difficulties are bypassed in the case of isotropic elasticity using logarithmic strains and the exponential mapping. In isotropic elasticity the stress and elastic strain tensors commute and the Mandel stress tensor coincides with the rotated Kirchhoff stress tensor [1,5]. A physically motivated hyperelastic function of the logarithmic strains [16,17] may be employed. Retaining the linear term of the Taylor series of the exponential mapping for the integration of the plastic flow, a very simple algorithm is obtained [5], in which the large strains framework acts as a simple pre- and post-processor of the usual small strains algorithm, even for obtaining the algorithmic tangent [6]. It should be noted that with these algorithms any anisotropic yield function could be used and the plastic flow is computed using the corresponding small strains algorithm.

However, for the case of anisotropic elasticity, stresses and elastic strains do not commute in general and the dissipation equation presents major mathematical difficulties. Hence some researchers adopt formulations that rely on additive decompositions, see for example References [18,19], elastic isotropy [20–22] or other complex frameworks more difficult to implement in an implicit finite element code [23–26]; see also some criticisms in [27]. In summary, those algorithms do not retain the successful properties of the previously mentioned algorithms for isotropic elasticity.

The above-mentioned anisotropic elasto-plastic algorithms as well as the vast majority of the computational algorithms for anisotropic plasticity of continua do not take into account the possible evolution of the material symmetries. However, the evolution of the material symmetries with non-proportional plastic strains is intuitive and has been observed experimentally, see for example References [28–32]. This evolution is closely related to the texture evolution of the microstructure, also observed experimentally, see for example References [33–43]. Texture evolution involves both changes in the yield function and in the preferred directions. In practice, as a first approximation, the yield function evolution may be taken into account through isotropic and kinematic hardening of the original anisotropic yield function. This approximation has given good results [21,22,28,32,44,45], even if constant normalized parameters of the Hill yield function are used for a wide range of plastic strains [9,32].

For an accurate simulation, the rotation of the preferred directions must also be taken into account. In crystal plasticity, the lattice rotation and the plastic spin are closely related by the Schmidt law. In continuum plasticity, the physical meaning of the plastic spin has been much discussed even

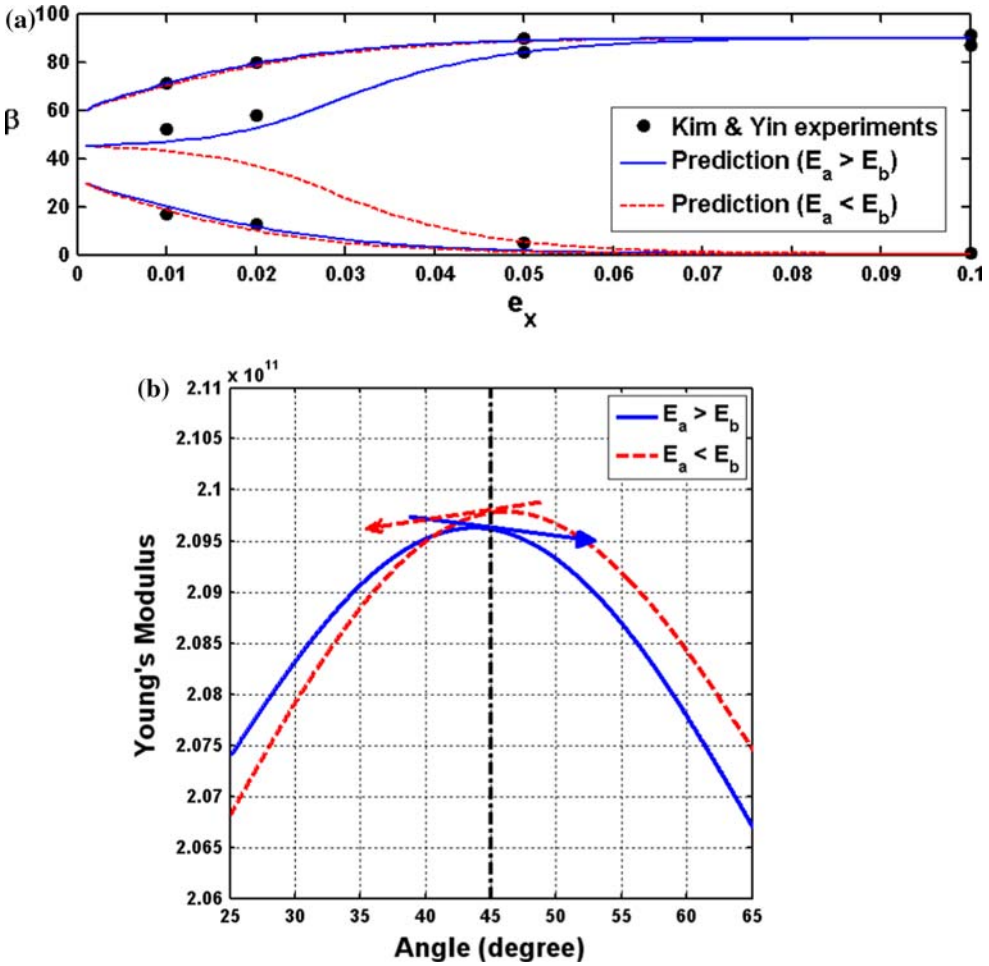

Fig. 2 The effect of the elastic anisotropy. **a** The evolution of the principal orthotropic directions, **b** Young's modulus at different angles with respect to the rolling direction (a-direction). $E_a = 204$ GPa and $E_b = 203$ GPa are used for the *solid lines* while $E_a = 203$ GPa and $E_b = 204$ GPa are used for the *dashed lines* where a and b represent the rolling direction and the transverse direction of a metal sheet, respectively. See Table 1 for the other elastic constants which are the same for both cases

for the case of isotropic elasticity, see for example [46–51]. The usual choice in isotropic elasticity is a vanishing plastic spin. This is a natural choice for isotropic elasticity because the plastic spin does not appear in the dissipation equation and does not affect the stored or dissipated energies [9]. Indeed, since there is no preferred orientation, on average, the microstructure should not show any rotation preference. However, in the case of elastic anisotropy, the stress tensor in the dissipation equation is the unsymmetric Mandel stress tensor, which produces work on the plastic spin, and hence needs to be accounted for in the energy balance equations. In addition, the evolution of the material symmetries also produces a change in the stored energy in the case of anisotropy. In [9], a framework for anisotropic elasto-plasticity using logarithmic strains, the multiplicative decomposition and the exponential mapping is presented. The model takes into account the evolution of the orthotropic preferred directions and was shown to predict the experimental results of Reference [32] for material symmetry evolution. These simulations are also used in this paper to gain further insight into the meaning of the material parameters. Central to the model is the importance of the evolution of the preferred directions and the effect on both the stored energy and the dissipation terms. This is an important difference with other works in which such evolution is also taken into account but through ad-hoc constitutive equations for the plastic spin [21,22,32,44,45].

In this paper, we present results of some studies on the model of Reference [9] in order to obtain deeper insight into the use of the parameters for the constitutive equations and the effects that may be simulated, as for example the cross effect during path changes on the plastic strains.

In the following, we first outline the main features of the model of Reference [9], focusing on the rotation of the

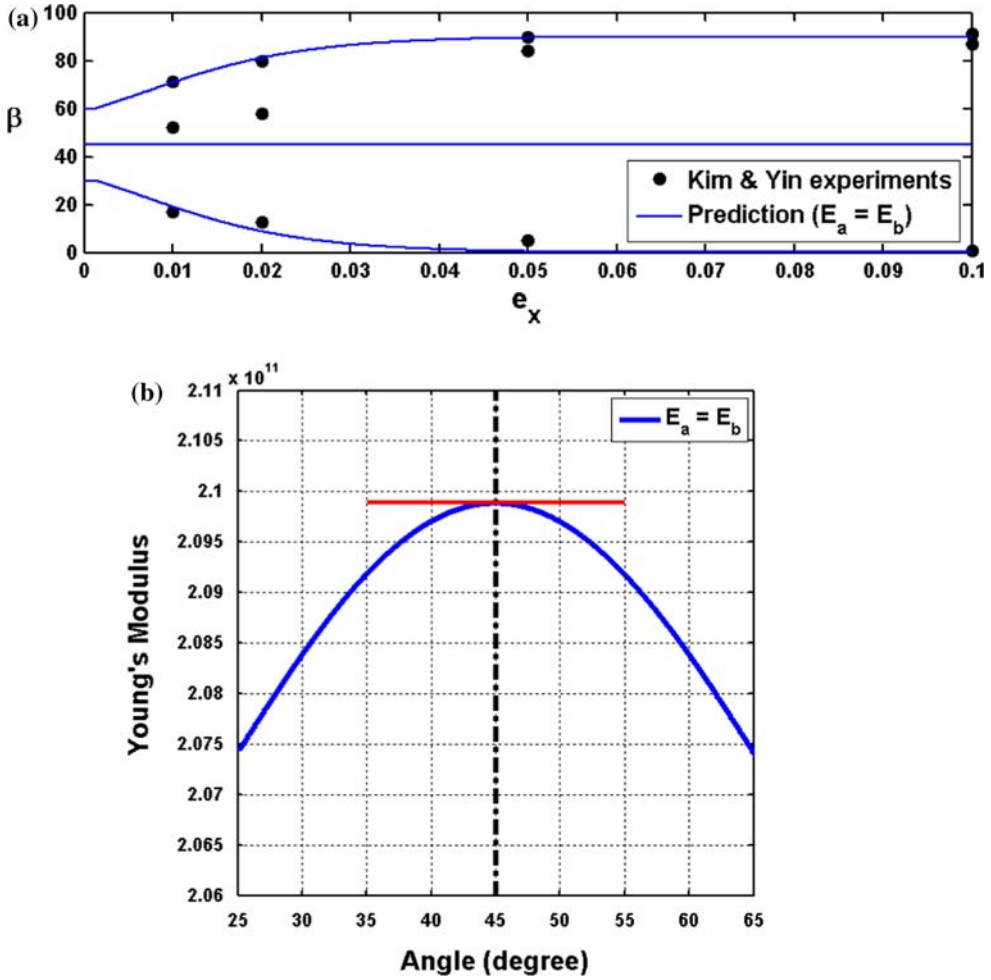

Fig. 3 The effect of the elastic anisotropy. **a** The evolution of the principal orthotropic directions, **b** Young's modulus at different angles with respect to the rolling direction (a-direction). $E_a = E_b = 204\,\text{GPa}$

orthotropic directions. Next, we discuss the effect of the parameters on the predictions with physical interpretations and give some results comparing with physical test data. For a constitutive model, a simple procedure to obtain the material parameters is always desirable. We present a procedure to obtain the spin parameters from Lankford *R*-values and the predictions are compared to those of Reference [44]. Thereafter, we give some results regarding the predictability of the model in nonproportional loading conditions. Finally, in the last section of the paper, we present our conclusions of this work.

2 The Montáns-Bathe model

In this section, we review the ingredients of the Montáns-Bathe model. A detailed description is given in [9]. We follow the notation of [1,3].

2.1 Kinematics

The model is based on the Lee decomposition which leads to the following multiplicative decomposition for the deformation gradient

$$ {}^{t}_{0}\boldsymbol{X} = {}^{t}_{0}\boldsymbol{X}^{e}\ {}^{t}_{0}\boldsymbol{X}^{p} \tag{1} $$

where ${}^{t}_{0}\boldsymbol{X}$ is the deformation gradient and ${}^{t}_{0}\boldsymbol{X}^{e}$ and ${}^{t}_{0}\boldsymbol{X}^{p}$ represent its elastic and plastic part, respectively. The left superscript denotes always the current configuration while the left subscript represents the reference configuration. We will omit these left indices when confusion is hardly possible.

The spatial velocity gradient is

$$ \begin{aligned} {}^{t}\boldsymbol{l} &= {}^{t}_{0}\dot{\boldsymbol{X}}\ {}^{t}_{0}\boldsymbol{X}^{-1} \\ &= {}^{t}_{0}\dot{\boldsymbol{X}}^{e}({}^{t}_{0}\boldsymbol{X}^{e})^{-1} + {}^{t}_{0}\boldsymbol{X}^{e}\left[{}^{t}_{0}\dot{\boldsymbol{X}}^{p}({}^{t}_{0}\boldsymbol{X}^{p})^{-1}\right]({}^{t}_{0}\boldsymbol{X}^{e})^{-1} \end{aligned} \tag{2} $$

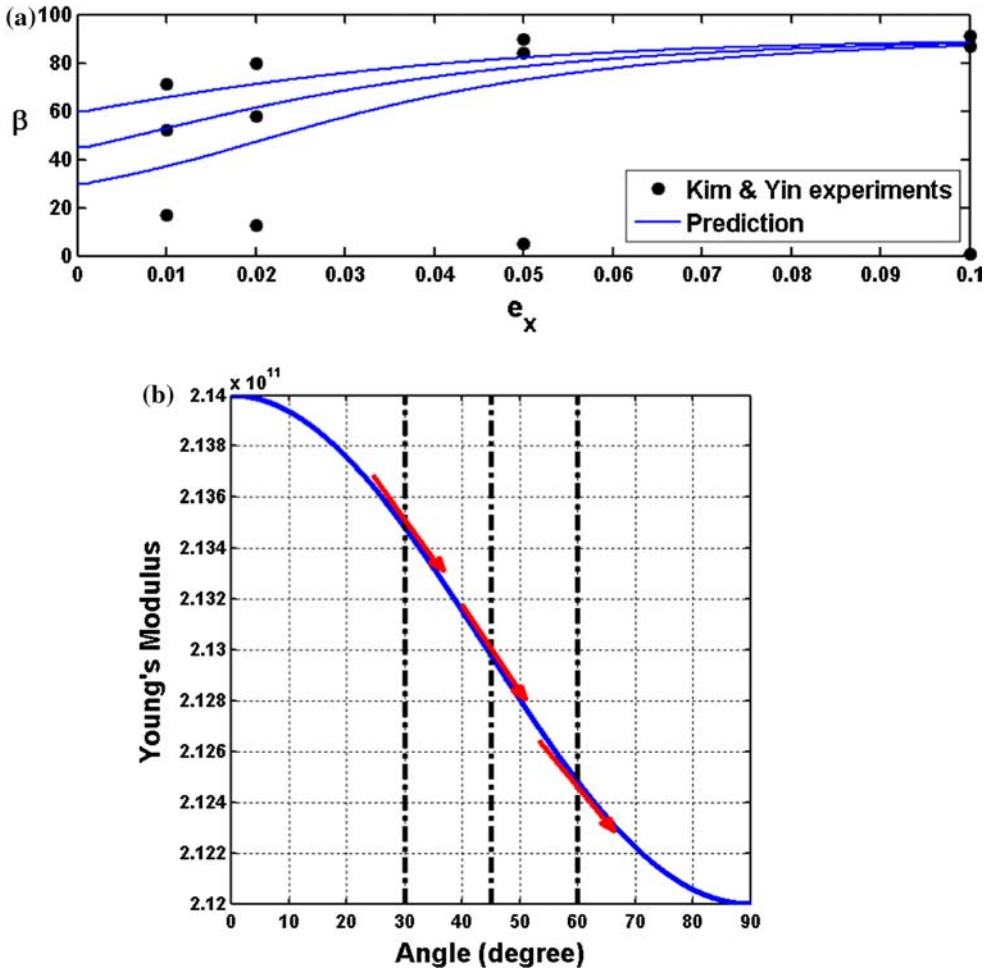

Fig. 4 The effect of the elastic anisotropy. **a** The evolution of the principal orthotropic directions, **b** Young's modulus at different angles with respect to the rolling direction (a-direction). $E_a = 214\,\text{GPa}$ and $E_b = 212\,\text{GPa}$

We use the modified plastic velocity gradient defined in the intermediate stress-free configuration

$$ {}^{t}\boldsymbol{L}^{p} = {}^{t}_{0}\dot{\boldsymbol{X}}^{p}({}^{t}_{0}\boldsymbol{X}^{p})^{-1} \tag{3} $$

whose symmetric part is the modified plastic deformation rate tensor ${}^{t}\boldsymbol{D}^{p}$ while its skew part is the modified plastic spin tensor ${}^{t}\boldsymbol{W}^{p}$.

Equation (3) provides the differential equation for the evolution of the plastic deformation gradient

$$ {}^{t}_{0}\dot{\boldsymbol{X}}^{p} = {}^{t}\boldsymbol{L}^{p}\,{}^{t}_{0}\boldsymbol{X}^{p} \tag{4} $$

whose backward-Euler exponential solution is given by

$$ {}^{t+\Delta t}_{0}\boldsymbol{X}^{p} = \exp(\Delta t\,{}^{t+\Delta t}\boldsymbol{L}^{p})\,{}^{t}_{0}\boldsymbol{X}^{p} \tag{5} $$

For small steps ($\|\Delta t\,{}^{t+\Delta t}\boldsymbol{L}^{p}\| \ll 1$, a typical restriction in plasticity formulations based on logarithmic strains), the exponential function can be approximated by

$$ \exp(\Delta t\,{}^{t+\Delta t}\boldsymbol{L}^{p}) \approx \exp(\Delta t\,{}^{t+\Delta t}\boldsymbol{D}^{p})\exp(\Delta t\,{}^{t+\Delta t}\boldsymbol{W}^{p}) \tag{6} $$

Then we have the following update formulas

$$ ({}^{t+\Delta t}_{0}\boldsymbol{X}^{p})^{-1} = ({}^{t}_{0}\boldsymbol{X}^{p})^{-1}\exp(-\Delta t\,{}^{t+\Delta t}\boldsymbol{W}^{p}) \times \exp(-\Delta t\,{}^{t+\Delta t}\boldsymbol{D}^{p}) \tag{7} $$

$$ {}^{t+\Delta t}_{0}\boldsymbol{X}^{e} = \boldsymbol{X}^{e}_{*}\exp(-\Delta t\,{}^{t+\Delta t}\boldsymbol{W}^{p})\exp(-\Delta t\,{}^{t+\Delta t}\boldsymbol{D}^{p}) \tag{8} $$

where $\boldsymbol{X}^{e}_{*} = {}^{t+\Delta t}_{t}\boldsymbol{X}\,{}^{t}_{0}\boldsymbol{X}^{e}$ is the trial elastic deformation gradient.

Now we define the incremental plastic rotation as

$$ {}^{t+\Delta t}_{t}\boldsymbol{R}^{w} = \exp(\Delta t\,{}^{t+\Delta t}\boldsymbol{W}^{p}) \tag{9} $$

Using Eqs. (8, 9) and the logarithm strains defined by $2\boldsymbol{E}^{e} = \ln\boldsymbol{C}^{e}$ where $\boldsymbol{C}^{e} = \boldsymbol{X}^{eT}\boldsymbol{X}^{e}$ is the right Cauchy-Green deformation tensor, we can derive the following update scheme for the strains (see details in [6])

$$ {}^{t+\Delta t}_{0}\underleftarrow{\boldsymbol{E}}^{e} \approx \underleftarrow{\boldsymbol{E}}^{e}_{*} - \Delta t\,{}^{t+\Delta t}\underleftarrow{\boldsymbol{D}}^{p} \tag{10} $$

We define $\underleftarrow{(\cdot)}$ as the quantity $(\cdot)$ rotated to the configuration where the plastic rotations are frozen during the plastic flow

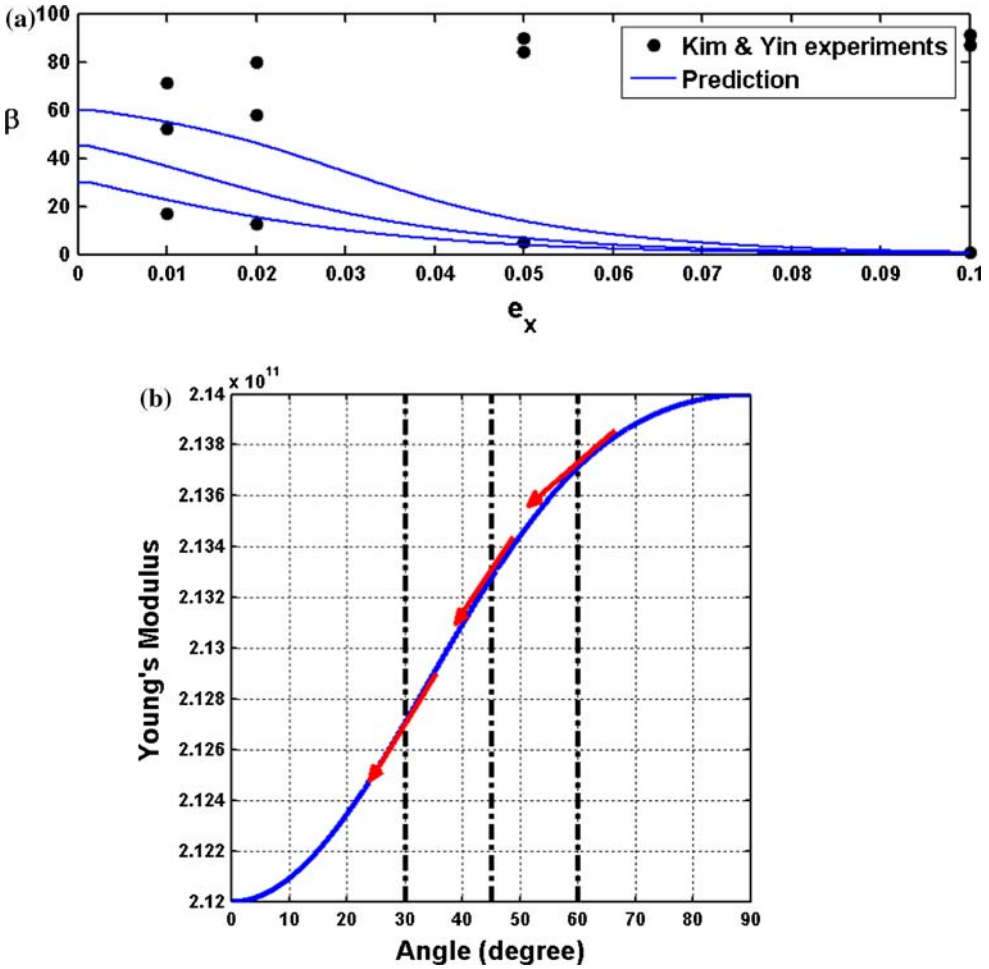

Fig. 5 The effect of the elastic anisotropy. **a** The evolution of the principal orthotropic directions, **b** Young's modulus at different angles with respect to the rolling direction (a-direction). $E_a = 212\,\text{GPa}$ and $E_b = 214\,\text{GPa}$

such that

$$\underset{\leftarrow}{(\cdot)} = {}^{t+\Delta t}_{t}\boldsymbol{R}^{wT}\,(\cdot)\,{}^{t+\Delta t}_{t}\boldsymbol{R}^{w} \tag{11}$$

Note that $\underset{\leftarrow}{\boldsymbol{E}}{}^{e}_{*}$ is given by the trial elastic deformation gradient, and ${}^{t+\Delta t}_{t}\boldsymbol{R}^{w}$ is not involved in Eq. (10) and only known after integrations.

2.2 Dissipation inequality

The stored energy function is assumed to be of the type

$$\mathcal{W} = \frac{1}{2}\boldsymbol{E}^{e} : \mathbb{A} : \boldsymbol{E}^{e} \tag{12}$$

where $\mathbb{A}$ is an elastic anisotropy tensor. Note that in Eq. (12) the strain tensor and the elastic anisotropy tensor are defined in the unrotated configuration where the elastic rotation is removed. During the plastic flow, this configuration and all objects defined in it rotate in each step by the amount ${}^{t+\Delta t}_{t}\boldsymbol{R}^{w}$ due to the plastic spin. However it has been observed that the anisotropy axes do not necessarily rotate as given by ${}^{t+\Delta t}_{t}\boldsymbol{R}^{w}$. Therefore we introduce an additional rotation for the anisotropy axes given by ${}^{t+\Delta t}_{t}\boldsymbol{R}^{A}$.

Then the rate of the stored energy function can be written as (for details see [9])

$$\dot{\mathcal{W}} = \underset{\leftarrow}{\boldsymbol{T}} : \underset{\leftarrow}{\dot{\boldsymbol{E}}}{}^{e} + \underset{\leftarrow}{\boldsymbol{T}}_{w} : \underset{\leftarrow}{\boldsymbol{W}}{}^{A} = \boldsymbol{T} : \underset{\leftarrow}{\mathcal{L}}\boldsymbol{E}^{e} + \boldsymbol{T}_{w} : \boldsymbol{W}^{A} \tag{13}$$

where $\boldsymbol{T} = \mathbb{A} : \boldsymbol{E}^{e}$ is a symmetric tensor defined as a generalized Kirchhoff stress tensor which is work conjugate to the logarithmic strains, $\boldsymbol{T}_{w} = \boldsymbol{E}^{e}\boldsymbol{T} - \boldsymbol{T}\boldsymbol{E}^{e}$ is a skew tensor, $\boldsymbol{W}^{A} = \dot{\boldsymbol{R}}^{A}(\boldsymbol{R}^{A})^{T}$ is a spin tensor for the anisotropy axes, and $\underset{\leftarrow}{\mathcal{L}}(\cdot)$ is a Lie derivative with ${}^{t+\Delta t}_{t}\boldsymbol{R}^{w}$ acting as a gradient.

Similarly we assume the following expression for the rate of the hardening potential

$$\begin{aligned}\dot{\mathcal{H}} &= \underset{\leftarrow}{\boldsymbol{B}}_{s} : \underset{\leftarrow}{\dot{\boldsymbol{E}}}{}^{i} + \underset{\leftarrow}{\boldsymbol{B}}_{w} : \underset{\leftarrow}{\boldsymbol{W}}{}^{H} + \kappa\dot{\zeta} + \kappa_{w}\dot{\xi} \\ &= \boldsymbol{B}_{s} : \underset{\leftarrow}{\mathcal{L}}\boldsymbol{E}^{i} + \boldsymbol{B}_{w} : \boldsymbol{W}^{H} + \kappa\dot{\zeta} + \kappa_{w}\dot{\xi}\end{aligned} \tag{14}$$

where $\boldsymbol{B}_{s}$ is the backstress tensor, $\boldsymbol{E}^{i}$ are logarithmic strain-like internal variables and $\boldsymbol{B}_{w} = \boldsymbol{E}^{i}\boldsymbol{B}_{s} - \boldsymbol{B}_{s}\boldsymbol{E}^{i}$, the tensor $\boldsymbol{W}^{H}$ is the spin for the hardening anisotropy axes, the scalars κ

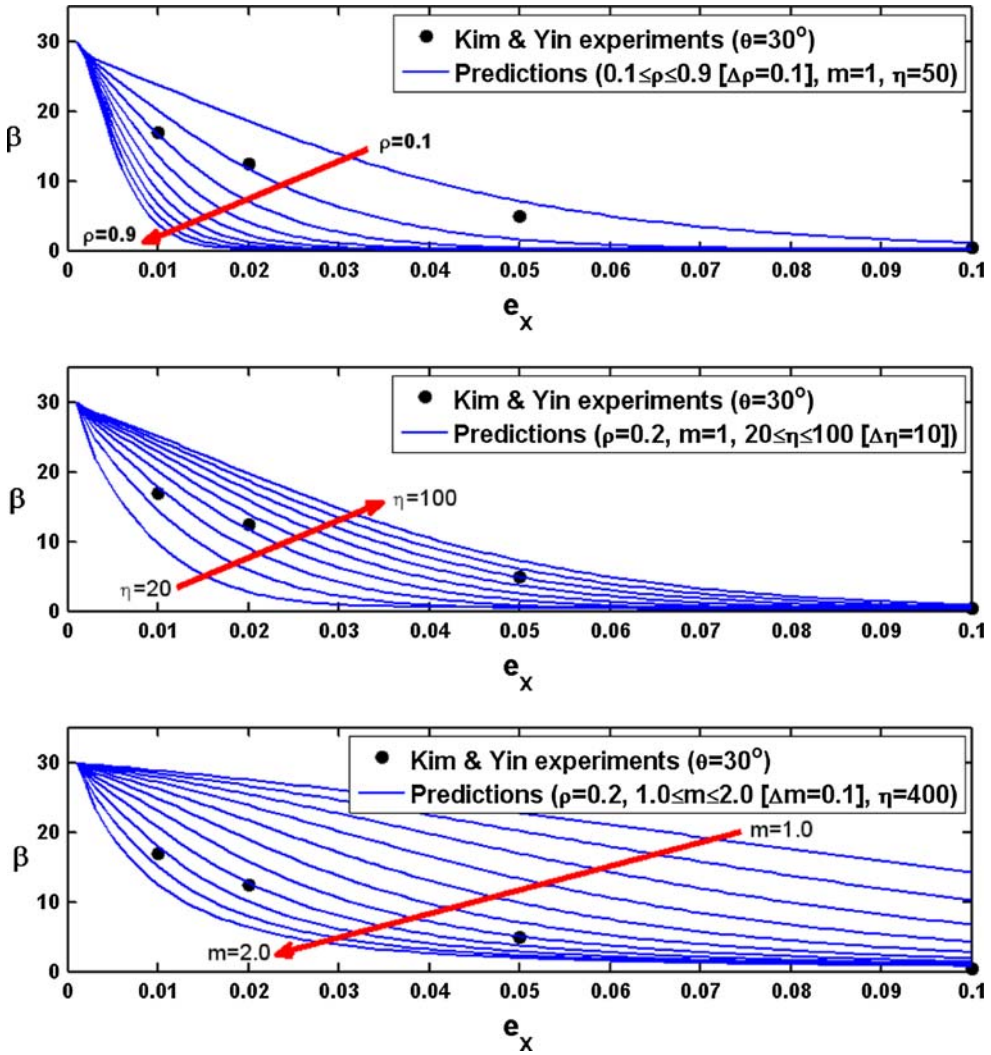

Fig. 6 The effect of parameters on the evolution of the principal orthotropic directions. θ is the initial orientation of the orthotropic axis

Table 1 The material parameters used in Sect. 3

Elastic constants	Hill's yield function parameters	Hardening
$E_a = 204\,\text{GPa}$		
$E_b = 203\,\text{GPa}$	$f = 0.3613$	$M = 1.0$
$E_c = 210\,\text{GPa}$	$h = 0.4957$	$\kappa_0 = 230.00\,\text{MPa}$
$\nu_{ab} = \nu_{ac} = \nu_{bc} = 0.3$	$g = 0.3535$	$\kappa_\infty = 276.00\,\text{MPa}$
$G_{ab} = 82\,\text{GPa}$	$l = 1.0$	$\delta = 30$
$G_{ac} = G_{bc} = 80.77\,\text{GPa}$		$\bar{h} = 350\,\text{MPa}$

and κ_w are the effective stress-like internal variables (current yield stress and couple-stress, respectively) and the scalars ζ and ξ (effective plastic strain and effective plastic rotation) are the effective strain-like internal variables. For the evolution of the yield stress and the backstress, we use Prager's hardening model with the SPM (Splitting of Plastic Modulus) method, see [4], including the possibility of anisotropic kinematic hardening given by

$$\begin{aligned}\kappa &= (1-M)\kappa_0 + M\bar{\kappa} \\ &= (1-M)\kappa_0 + M\left[\kappa_\infty - (\kappa_\infty - \kappa_0)\exp(-\delta\zeta) + \bar{h}\zeta\right] \end{aligned} \tag{15}$$

$$\underset{\leftarrow}{\dot{\boldsymbol{B}}}_s = \frac{2}{3}(1-M)\frac{d\bar{\kappa}}{d\zeta}\,\underset{\leftarrow}{\mathbb{H}} : \underset{\leftarrow}{\boldsymbol{D}}^p \tag{16}$$

where M is the mixed hardening parameter, $\mathbb{H}$ is an anisotropy tensor for the kinematic hardening and κ_∞, κ_0, δ and $\bar{h}$ are material properties which govern the isotropic hardening curve.

Then the dissipation inequality becomes

$$\begin{aligned}\dot{\mathcal{D}}^p = {} & \boldsymbol{\Xi}_s : \boldsymbol{D}^p + \boldsymbol{\Xi}_w : \boldsymbol{W}^d - \boldsymbol{B}_s : \underset{\leftarrow}{\mathcal{L}E}^i - \boldsymbol{B}_w : \boldsymbol{W}^H \\ & - \kappa\dot{\zeta} - \kappa_w\dot{\xi} \;\geq 0 \end{aligned} \tag{17}$$

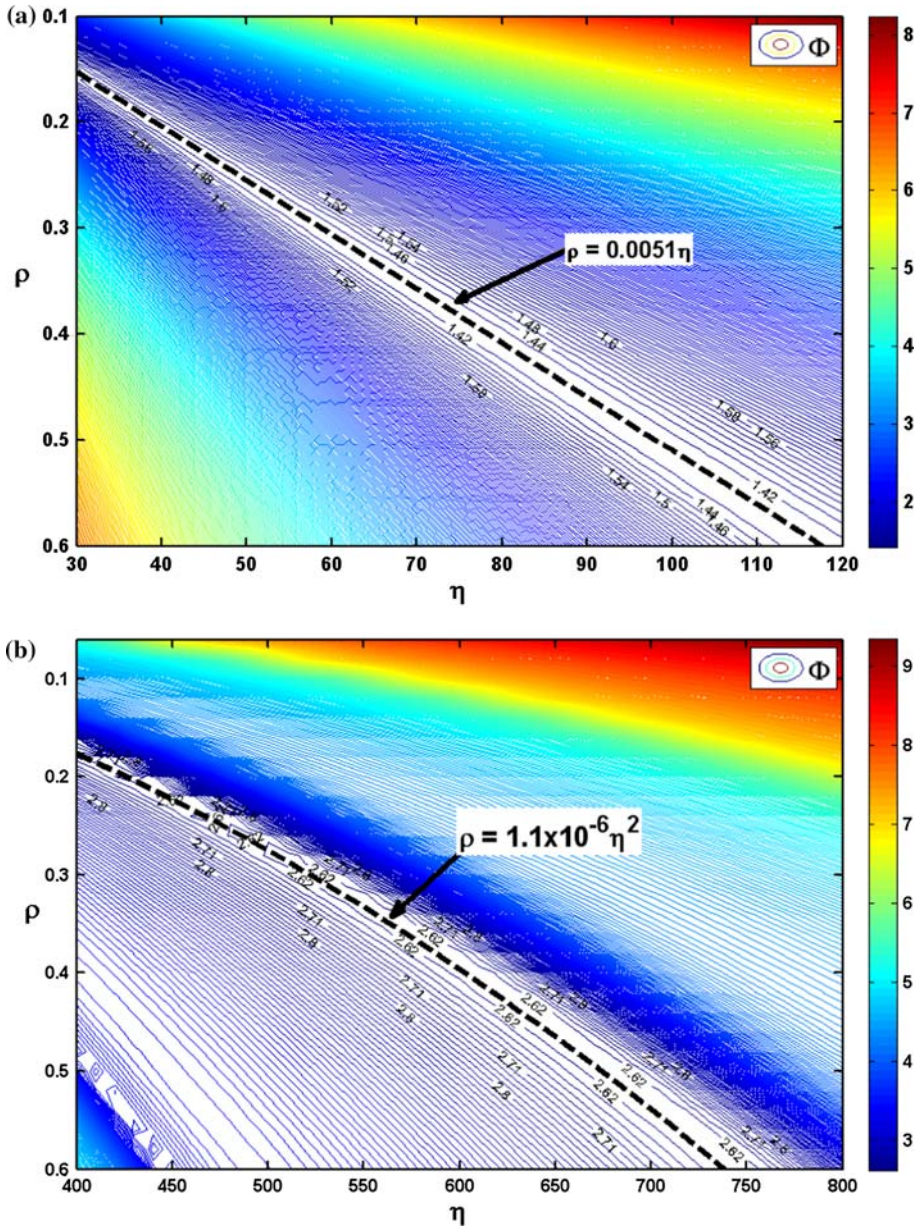

Fig. 7 Contour maps for Φ with respect to ρ and η. **a** $m = 1$, **b** $m = 2$. The *dashed lines* represent where the change of Φ is minimum

where $\boldsymbol{\Xi}_s$ and $\boldsymbol{\Xi}_w$ are the symmetric part and the skew part of the Mandel stress tensor $\boldsymbol{\Xi} = \boldsymbol{C}^e\boldsymbol{S}$ (where $\boldsymbol{S}$ is the pull-back of the Kirchhoff stress $\boldsymbol{\tau}$ to the stress-free configuration), respectively and $\boldsymbol{W}^d = \boldsymbol{W}^p - \boldsymbol{W}^A$ is the dissipative spin tensor. The symmetric part and the skew part of the Mandel stress tensor can be related to the generalized Kirchhoff stress tensor by

$$\boldsymbol{\Xi}_s = \boldsymbol{T} : \mathbb{S}^M \tag{18}$$

$$\boldsymbol{\Xi}_w = \boldsymbol{T}_w = \boldsymbol{E}^e\boldsymbol{T} - \boldsymbol{T}\boldsymbol{E}^e \tag{19}$$

where $\mathbb{S}^M$ is the fourth order mapping tensor which for small elastic strains is close to the identity tensor.

We assume that, without loss of generality, the elastic region is enclosed by two yield functions $f_s(\boldsymbol{\Xi}_s, \boldsymbol{B}_s, \kappa)$ and $f_w(\boldsymbol{\Xi}_w, \boldsymbol{B}_w, \kappa_w)$. Then the Lagrangian for the constrained problem is $L = \dot{\mathcal{D}}^p - \dot{\imath} f_s - \dot{\gamma} f_w$ where $\dot{\imath}$ and $\dot{\gamma}$ are the consistency parameters. By claiming that the principle of maximum dissipation holds ($\nabla L = 0$), we have the associated flow and hardening rules given by

$$\begin{cases} \dfrac{\partial L}{\partial \boldsymbol{\Xi}_s} = 0 \Rightarrow \boldsymbol{D}^p = \dot{\imath}\dfrac{\partial f_s}{\partial \boldsymbol{\Xi}_s} \quad \text{and} \quad \dfrac{\partial L}{\partial \boldsymbol{\Xi}_w} = 0 \Rightarrow \boldsymbol{W}^d = \dot{\gamma}\dfrac{\partial f_w}{\partial \boldsymbol{\Xi}_w} \\ \dfrac{\partial L}{\partial \boldsymbol{B}_s} = 0 \Rightarrow \underset{\leftarrow}{\mathcal{L}}\boldsymbol{E}^i = -\dot{\imath}\dfrac{\partial f_s}{\partial \boldsymbol{B}_s} \text{ and } \dfrac{\partial L}{\partial \boldsymbol{B}_w} = 0 \Rightarrow \boldsymbol{W}^H = -\dot{\gamma}\dfrac{\partial f_w}{\partial \boldsymbol{B}_w} \\ \dfrac{\partial L}{\partial \kappa} = 0 \Rightarrow \dot{\zeta} = -\dot{\imath}\dfrac{\partial f_s}{\partial \kappa} \quad \text{and} \quad \dfrac{\partial L}{\partial \kappa_w} = 0 \Rightarrow \dot{\xi} = -\dot{\gamma}\dfrac{\partial f_w}{\partial \kappa_w} \end{cases} \tag{20}$$

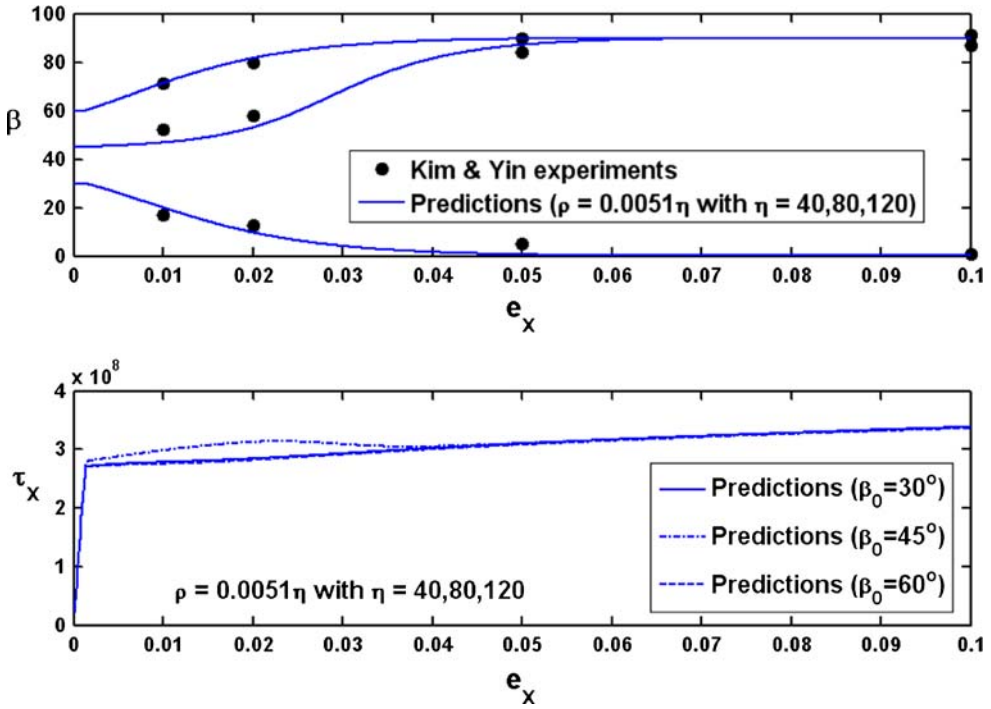

Fig. 8 The evolution of the orthotropic axes and the flow stresses. Pairs of ρ and η on the *dashed line* in Fig. 7a are used with $m = 1$

2.3 Yield functions

We assume that the well-known Hill's quadratic yield criterion holds for the symmetric part of the Mandel stress tensor.

$$f_s = \frac{3}{2\kappa^2}(\boldsymbol{\Xi}_s - \boldsymbol{B}_s) : \mathbb{A}_s^p : (\boldsymbol{\Xi}_s - \boldsymbol{B}_s) - 1 = 0 \tag{21}$$

where $\mathbb{A}_s^p$ is the plastic anisotropy tensor assumed to have the same anisotropy directions as the elastic anisotropy tensor. Note that $\mathbb{A}_s^p$ extracts the deviatoric stresses only and therefore the mean stresses do not enter the yield condition in Eq. (21). From Eq. (20), we have

$$\underset{\leftarrow}{\mathcal{L}}\boldsymbol{E}^i = \boldsymbol{D}^p = \frac{3}{\kappa^2}\mathbb{A}_s^p : (\boldsymbol{\Xi}_s - \boldsymbol{B}_s)\,\dot{t} \tag{22}$$

$$\dot{\zeta} = \frac{2}{\kappa}\dot{t} \tag{23}$$

where $f_s = 0$ at yield is used in Eq. (23).

On the other hand, the von Mises type of yield function is used for the skew part in this study

$$f_w = \|\boldsymbol{\Xi}_w\| - \sqrt{2}\kappa_w \tag{24}$$

where κ_w is the allowed yield value which may be set to zero. Then we have also from Eq. (20)

$$\boldsymbol{W}^d = \dot{\gamma}\,\hat{\boldsymbol{\Xi}}_w \tag{25}$$

$$\dot{\xi} = \sqrt{2}\dot{\gamma} \tag{26}$$

where $\hat{\boldsymbol{\Xi}}_w = \boldsymbol{\Xi}_w/\|\boldsymbol{\Xi}_w\|$.

Note that Eq. (24) indicates that the plastic spin will take place once $\|\boldsymbol{\Xi}_w\|$ becomes larger than $\sqrt{2}\kappa_w$ regardless of the symmetric part of the plastic flow. However, this is inconsistent with experimental observations where a progressive rotation of the anisotropy axes is measured. Furthermore, in crystal plasticity the Schmidt law shows a clear relation between the plastic deformation rate tensor and the plastic spin tensor. Hence we propose the following relationship connecting the skew part with the symmetric part.

$$\dot{\xi} = \left(\frac{\langle f_w \rangle}{\eta}\right)^m \dot{\zeta} \tag{27}$$

where $\langle\cdot\rangle$ is the Macauley bracket function and η and m are material properties with η having the unit of stress. This viscoplastic-like law relates the plastic spin to the magnitude of the skew part of the Mandel stress tensor, and there is naturally no plastic spin when the skew part of the Mandel stress is zero (as usually assumed in isotropic plasticity).

3 Parametric study

We present in this section, some parametric studies to obtain insight into the model. We discuss the physical meaning of the results and the effects that the material parameters for the skew part have on the predictions in some loading cases.

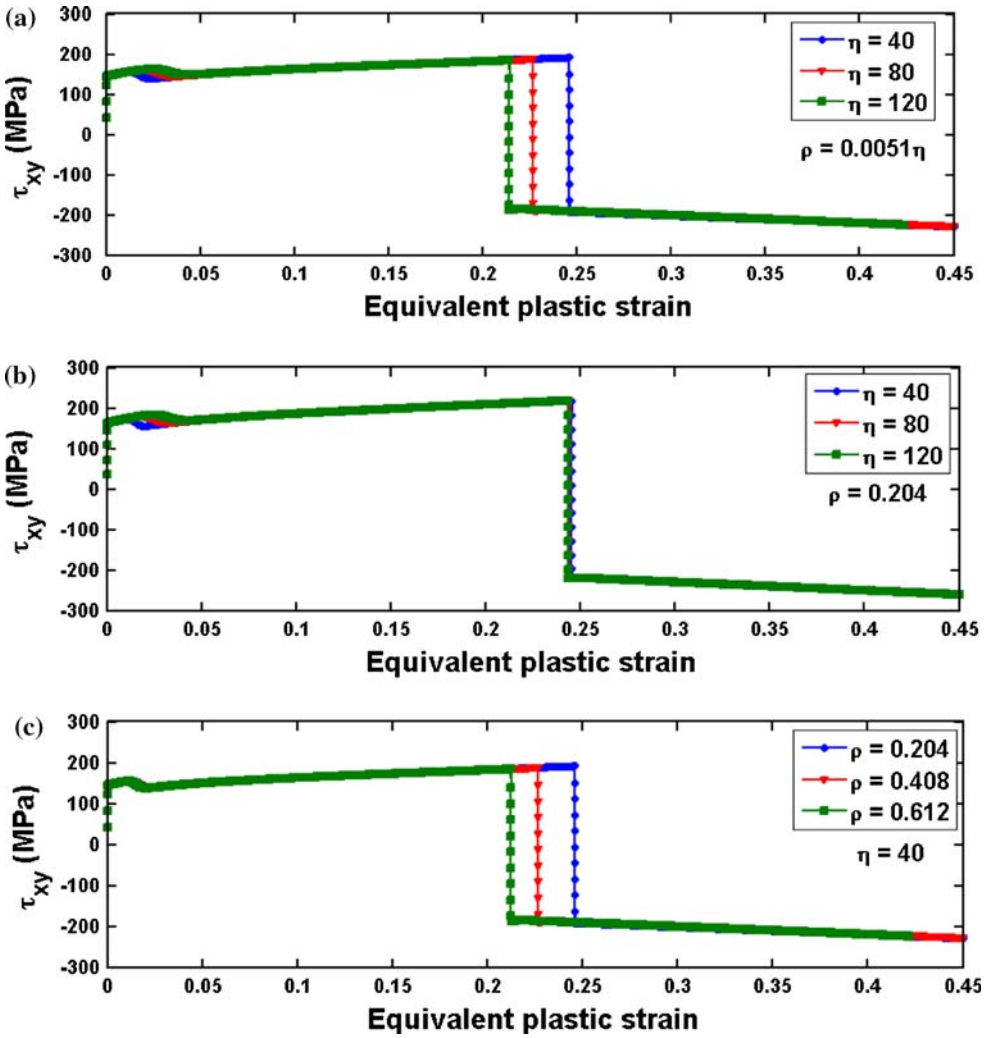

Fig. 9 The evolution of shear stress in a reverse simple shear test ($m = 1$) **a** with pairs of ρ and η shown as the *dashed line* in Fig. 7a; **b** with the fixed $\rho = 0.204$; **c** with the fixed $\eta = 40$

3.1 Constitutive equation for spin tensors

We assume the following constitutive equations for the spin tensors

$$\boldsymbol{W}^{axes} = \boldsymbol{W}^p + \boldsymbol{W}^A = -\rho \boldsymbol{W}^d \tag{28}$$

where $\boldsymbol{W}^{axes}$ is the total spin of the anisotropy axes with respect to the unrotated configuration (where the elastic rotation is removed).

Then, from $\boldsymbol{W}^d = \boldsymbol{W}^p - \boldsymbol{W}^A$, we have

$$\boldsymbol{W}^p = \frac{1}{2}(1-\rho)\boldsymbol{W}^d \tag{29}$$

$$\boldsymbol{W}^A = -\frac{1}{2}(1+\rho)\boldsymbol{W}^d \tag{30}$$

Equation (28) implies that the spin of the anisotropy axes is proportional to the dissipative spin. In general ρ may be better modeled to be a function of the plastic deformation, but here we assume, as a first approximation, that ρ is constant. Note that the definition of ρ is slightly modified from the original definition proposed in [9].

We are able to establish a proper range of ρ based on physical reasoning.

First we claim that the anisotropy axes rotate to a more favorable orientation after plastic flow such that the stored strain energy decreases. Therefore the second term in Eq. (13), which corresponds to the change in internal energy due to the anisotropy axes rotation, must be negative. This leads to, using Eqs. (25) and (30),

$$\boldsymbol{T}_w : \boldsymbol{W}^A = -\frac{1}{2}(1+\rho)\dot{\gamma}\,\|\boldsymbol{\Xi}_w\| < 0 \tag{31}$$

Since $\dot{\gamma}$ and $\|\boldsymbol{\Xi}_w\|$ are always positive, we have

$$\rho > -1 \tag{32}$$

Table 2 The material parameters used in Sect. 4

Material	Elastic constants	R-values	Hardening	Spin
DDQ-1	$E_a = 212\,\text{GPa}$	$R_0 = 2.722$	$M = 0.8$	$\rho = 0.40$
	$E_b = 208\,\text{GPa}$	$R_{45} = 1.474$	$\kappa_0 = 152.00\,\text{MPa}$	$\eta = 60$
	$E_c = 210\,\text{GPa}$	$R_{90} = 2.169$	$\kappa_\infty = 387.81\,\text{MPa}$	$m = 1.0$
	$\nu_{ab} = \nu_{ac} = \nu_{bc} = 0.3$		$\delta = 9.23, \bar{h} = 0.0$	
	$G_{ab} = 82\,\text{GPa}$		$h_a^E = h_b^E = h_c^E = 1.0$	
	$G_{ac} = G_{bc} = 80.77\,\text{GPa}$		$h_{ab}^G = h_{ac}^G = h_{bc}^G = 1.6$	
DDQ-2	$E_a = 208\,\text{GPa}$	$R_0 = 2.137$	$M = 0.8$	$\rho = 0.26$
	$E_b = 212\,\text{GPa}$	$R_{45} = 0.930$	$\kappa_0 = 152.22\,\text{MPa}$	$\eta = 20$
	$E_c = 210\,\text{GPa}$	$R_{90} = 1.508$	$\kappa_\infty = 372.23\,\text{MPa}$	$m = 1.0$
	$\nu_{ab} = \nu_{ac} = \nu_{bc} = 0.3$		$\delta = 7.87, \bar{h} = 0.0$	
	$G_{ab} = 82\,\text{GPa}$		$h_a^E = h_b^E = h_c^E = 1.0$	
	$G_{ac} = G_{bc} = 80.77\,\text{GPa}$		$h_{ab}^G = h_{ac}^G = h_{bc}^G = 5.0$	
DQ	$E_a = 182\,\text{GPa}$	$R_0 = 1.600$	$M = 0.8$	$\rho = 0.48$
	$E_b = 178\,\text{GPa}$	$R_{45} = 1.010$	$\kappa_0 = 198.00\,\text{MPa}$	$\eta = 60$
	$E_c = 180\,\text{GPa}$	$R_{90} = 1.460$	$\kappa_\infty = 455.00\,\text{MPa}$	$m = 1.0$
	$\nu_{ab} = \nu_{ac} = \nu_{bc} = 0.3$		$\delta = 9.95, \bar{h} = 0.0$	
	$G_{ab} = 70\,\text{GPa}$		$h_a^E = h_b^E = h_c^E = 1.0$	
	$G_{ac} = G_{bc} = 69.23\,\text{GPa}$		$h_{ab}^G = h_{ac}^G = h_{bc}^G = 2.2$	

Then we assume that the plastic spin has the same direction as the dissipative spin which physically means that the dissipative spin drives the plastic spin and consequently the spin of the unrotated configuration where the elastic rotation is removed. Hence, from Eq. (29), we have

$$\rho < 1 \tag{33}$$

Equations (32, 33) imply that the total spin of the anisotropy axes does not exceed the dissipative spin in magnitude, see Eq. (28).

Finally from Eqs. (25) and (28)

$$\boldsymbol{W}^{axes} = -\rho\dot{\gamma}\hat{\boldsymbol{\Xi}}_w \tag{34}$$

From this expression it is deduced that the anisotropy axes rotate in the direction of $\hat{\boldsymbol{\Xi}}_w$ if $\rho < 0$ while they rotate in the opposite direction of $\hat{\boldsymbol{\Xi}}_w$ if $\rho > 0$. It is reasonable to postulate that the anisotropy axes will rotate in the opposite direction of $\hat{\boldsymbol{\Xi}}_w$ because $\boldsymbol{\Xi}_w$ measures how much the elastic strain tensor and the stress tensor are not coaxial. This can be also confirmed by numerical tests versus laboratory test data. Consider the data in Fig. 1, which shows the prediction for the evolution of the principal orthotropic directions and the comparison with the experimental result when a uniaxial tensile force is applied on a metal sheet with three initial orientations of orthotropic axes. We observe a rotation of the orthotropic axes to a wrong orientation when we use $\rho < 0$.

Hence, together with Eqs. (32) and (33), a reasonable range of ρ is

$$0 < \rho < 1 \tag{35}$$

3.2 The direction of axes rotation through elastic anisotropy

Boehler and Koss [31] and Kim and Yin [32] performed similar experiments to measure the evolution of orthotropic axes of a metal sheet under uniaxial tension with initial off-axis loading angles of 30°, 45° and 60°. Their results are qualitatively the same except for the case in which the initial off-axis loading angle is 45°. A counterclockwise rotation to 90° was observed by Kim and Yin while a clockwise rotation to 0° was reported by Boehler and Koss. Within our theory, these different observations can be explained by the elastic anisotropy because we claim that the anisotropy axes will rotate to more preferable directions such that the stored strain energy decreases. As shown in Fig. 2a, our model can predict both experimentally observed clockwise and counterclockwise rotations by controlling the elastic anisotropy. Hence we conclude that the difference between the two different experimental observations may be due to the unconsidered or unknown elastic anisotropies. Here we changed the Young's moduli slightly to have a different landscape of Young's modulus in the plane and in consequence of the

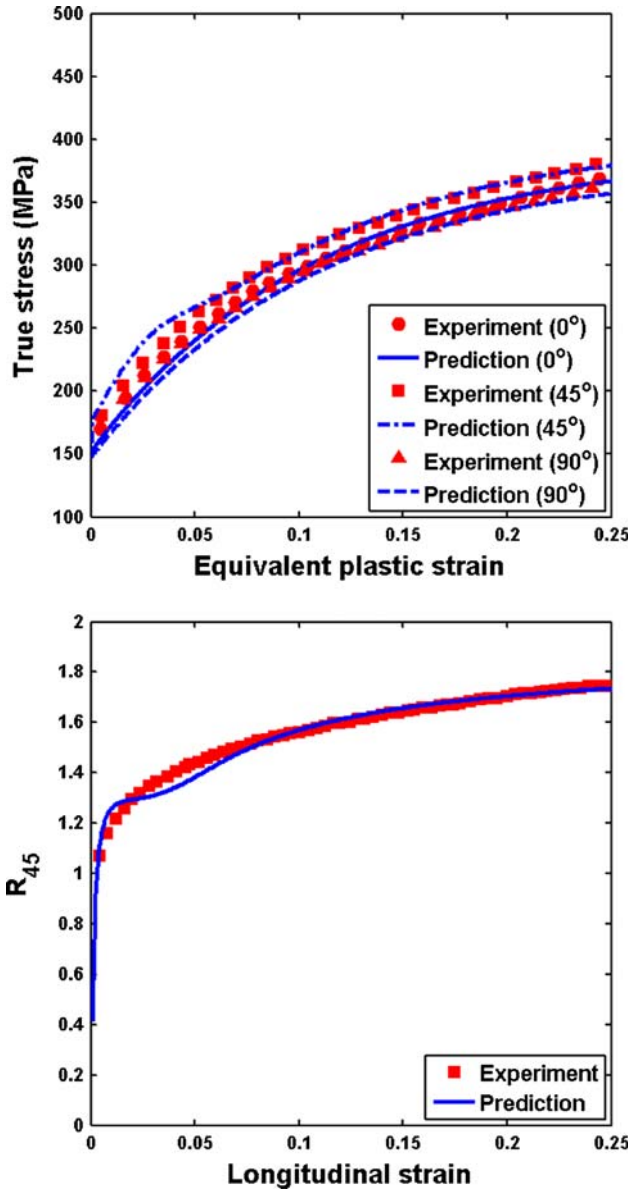

Fig. 10 The evolution of flow stresses and R_{45} for DDQ-1 in Table 2. The experimental results are taken from [44]

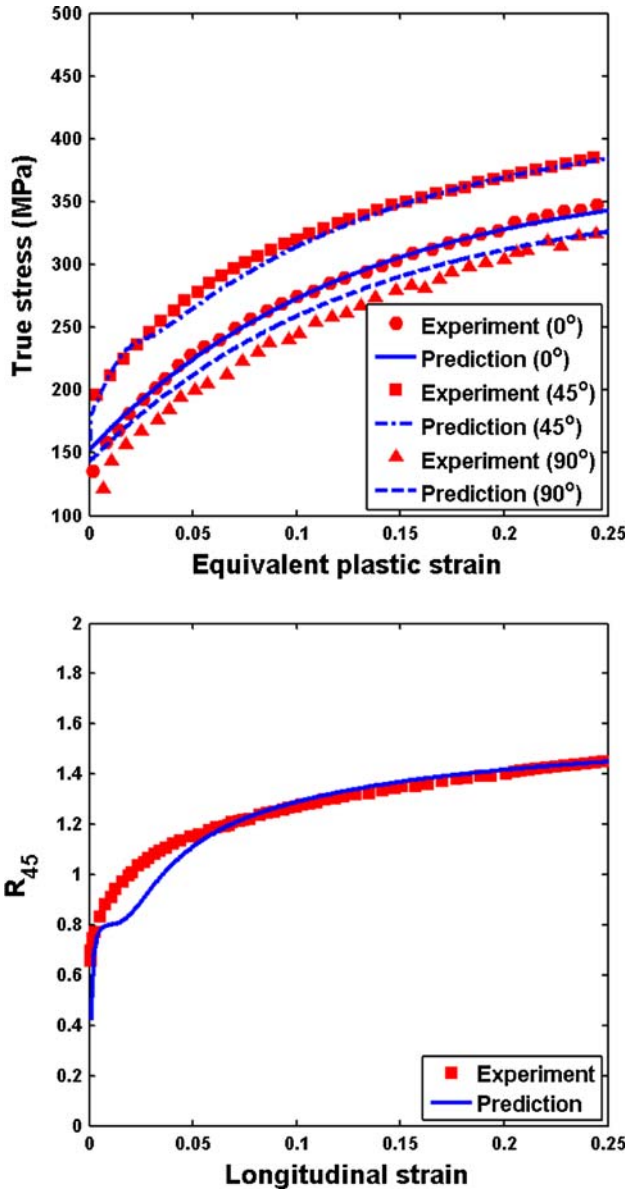

Fig. 11 The evolution of flow stresses and R_{45} for DDQ-2 in Table 2. The experimental results are taken from [44]

stored strain energy. Note that the orthotropic axes rotate in the direction of the downhill in Young's modulus variation, see Fig. 2b. If we select an elastic tensor such that the Young's modulus variation has a zero slope at 45°, no rotation takes place for an initial orientation of 45° as shown in Fig. 3. Moreover the model predicts that the orthotropic axes rotate to 0° or 90° regardless of its initial orientation if the Young's modulus has a monotonic increasing or decreasing pattern, see Figs. 4 and 5. Therefore the elastic anisotropy is very important in our model and enriches the model's predictability. This is a key feature of the model which distinguishes it from other phenomenological models that consider the plastic spin.

3.3 Sensitivity of the spin parameters

From Eqs. (23–29), the spin tensors can be rewritten as

$$\boldsymbol{W}^A = -\frac{1}{2\sqrt{2}}(1+\rho)\left(\frac{\langle f_w\rangle}{\eta}\right)^m \hat{\boldsymbol{\Xi}}_w\dot{\zeta} \tag{36}$$

$$\boldsymbol{W}^p = \frac{1}{2\sqrt{2}}(1-\rho)\left(\frac{\langle f_w\rangle}{\eta}\right)^m \hat{\boldsymbol{\Xi}}_w\dot{\zeta} \tag{37}$$

Figure 6 shows the effect of the spin parameters, ρ, η and m, on the evolution of the orthotropic axes in a uniaxial tension test. For the other material constants, we use the same values as in [9] and they are listed in Table 1.

To be more quantitative in the analysis, we define the following root mean square errors for the orientation of the orthotropic axes

$$\Phi = \frac{1}{3}\left(\Theta_{\beta_0=30^\circ} + \Theta_{\beta_0=45^\circ} + \Theta_{\beta_0=60^\circ}\right) \tag{38}$$

where

$$\Theta_{\beta_0} = \sqrt{\frac{1}{n}\sum_{i=1}^{n}\left(\beta_i^{\exp} - \beta_i^{\text{num}}\right)^2} \tag{39}$$

Here $\beta_i^{\exp}$ is the angle between the orthotropic axis (the rolling direction) and the loading direction obtained from experiments while β_i^{num} is the predicted angle by the model, β_0 is the initial orientation of the orthotropic axis and n is the number of experimental data points. Here the experimental data obtained by Kim and Yin [32] are used as a reference. The dimension for the angle is degree.

Figure 7 shows the contour plot for Φ with respect to ρ and η when $m = 1, 2$. We can see that there is a region where the change of Φ is negligible, which means that there is a certain relationship between ρ and η which gives a very similar prediction for the anisotropic axes rotation. These relationships obtained from the simulations for each m are also shown in Fig. 7 as dashed lines with their equations. The simulation results with some pairs of ρ and η on the dashed line for $m = 1$ are shown in Fig. 8. Note that almost the same predictions are obtained not only for the evolution of the anisotropic axes but also for the evolution of the flow stresses.

This can be explained by considering the total spin of the anisotropic axes with respect to the unrotated configuration in Eq. (28). From Eqs. (28), (36) and (37), we have

$$\boldsymbol{W}^{axes} = -\frac{1}{\sqrt{2}}\left(\frac{\rho}{\eta^m}\right)\langle f_w\rangle^m\,\hat{\boldsymbol{\Xi}}_w\dot{\xi} \tag{40}$$

This indicates that the ratio of ρ to η^m may play a more important role in the evolution of the anisotropic axes than the specific values of ρ, η and m. If we set the ratio to be a constant C, we have

$$\rho = C\eta^m \tag{41}$$

Equation (41) provides a possible relationship between the spin parameters. We see that the dashed lines in Fig. 7 correspond to $C = 0.0051$ for $m = 1$ and $C = 1.1 \times 10^{-6}$ for $m = 2$, respectively.

However each value of parameters, not only the ratio of them, may be important for certain problems. As an example, we performed a simulation of a simple shear deformation with a load reversal and the result is shown in Fig. 9. The same material properties are used as in the previous uniaxial tensile test. Different responses are obtained even when we use pairs of the spin parameters which satisfy the relationship shown in Fig. 7a. Especially, there is a clear

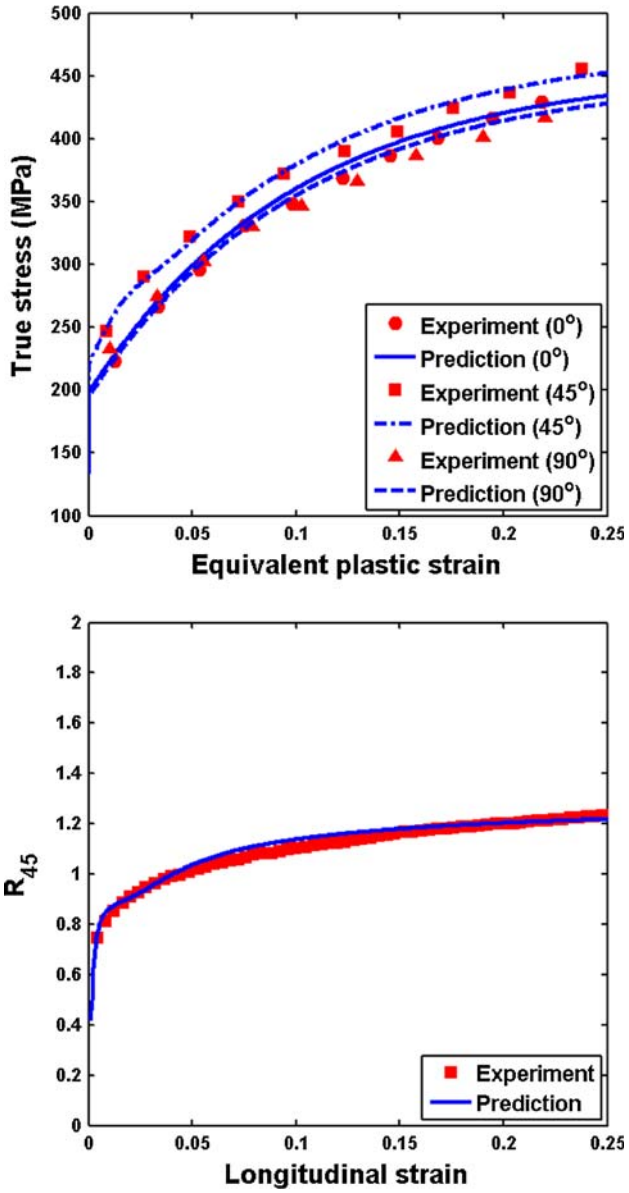

Fig. 12 The evolution of flow stresses and R_{45} for DQ in Table 2. The experimental results are adapted from [44]

difference in the amount of the equivalent plastic strain where the load reversal begins, see Fig. 9a. According to Fig. 9b,c, the change is mainly attributed to the value of the parameter ρ while η has a primary effect on the initial transient response which depends on the rate of anisotropic axes rotation. Note that, in principle, ρ determines the amount of the axes spin from the given dissipative spin while η scales the skew part of the Mandel stress tensor. Therefore each parameter has a unique function and each value of parameters, not only their ratio, may be important for a certain problem like in simple shear where the principal strain direction changes continuously during the plastic deformation and, in consequence, the orthotropic axes and the intermediate configurations do so too.

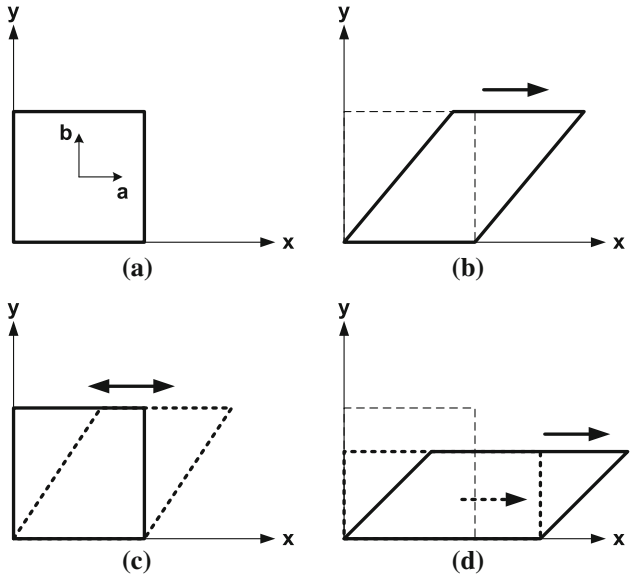

Fig. 13 The multi-paths loading problems. **a** Initial configuration where a and b represent the rolling direction and the transverse direction of a metal sheet, respectively; **b** The case of monotonic simple shear; **c** The case of reverse simple shear; **d** The case of tension-shear

4 Identification of spin parameters based on R-values

In general, spin parameters have been chosen in order that a model properly reproduces the evolution curve of anisotropic axes measured from the evolution of anisotropies in yield stress as in [32]. As an alternative, Choi et al. [44] recently proposed a possible way of identifying spin parameters based on the evolution of the R-values, also known as the Lankford coefficients. The motivation is based on the observation that the R-value shows a non-negligible evolution when an orthotropic axis is initially oriented at 45° while the R-values for the initial orientations of 0° and 90° can be regarded as constant, as usual. Also, it has been shown that the flow stress for the initial orientation of 45° will be over-predicted if a conventional hardening model is used without considering the axes rotation [44]. Therefore the rotation of the orthotropic axes in addition to a conventional hardening model needs to be included to predict the R-values and the flow stresses with better accuracy.

This procedure seems experimentally more practical than measuring the evolution of anisotropic axes directly because only uniaxial tensile test data for three different orientations of 0°, 45° and 90° are necessary. The experimental data for 0° and 90° are used to determine isotropic hardening parameters and then we use the evolution curves of the R-value and the flow stress for 45° to calibrate parameters for kinematic hardening and plastic spin. The coefficients of Hill's quadratic yield function are calculated from the reference R-values. Here we apply this procedure to our model and compare our predictions with the experimental results available in [44].

First of all, we need to clarify the definition of the R-value because it has been used in various forms in the literature. We use the same definition of the R-value as in [44] given by

$$R = \frac{\varepsilon_w}{\varepsilon_t} = -\frac{\varepsilon_w}{\varepsilon_l + \varepsilon_w} \tag{42}$$

where ε_l is the longitudinal strain in the direction of uniaxial loading, ε_t is the through-the-thickness strain and ε_w is the widthwise strain. Due to the difficulty in measuring ε_t of sheet metals, $\varepsilon_t = -(\varepsilon_l + \varepsilon_w)$ is used by assuming small elastic strains and incompressibility of the plastic strains.

It has been reported that the flow stress for initial orientation of 45° will be under-predicted when only isotropic hardening is used even if the axes rotation is considered. We need to include kinematic hardening. Since it is not our goal to discuss which hardening model is more adequate, we simply use Prager's mixed hardening rule as in Eqs. (15, 16) although Choi et al. [44] used a different hardening model. Of course, any kind of kinematic hardening model can be used with our model, simply by just replacing Eq. (16) with the chosen model equations. We use the orthotropic hardening tensor in Eq. (16), which in matrix form is

$$\overleftarrow{\mathbb{H}} = \begin{bmatrix} \frac{2}{3}h_a^E & -\frac{1}{3}\left(h_a^E + h_b^E - h_c^E\right) & -\frac{1}{3}\left(h_a^E - h_b^E + h_c^E\right) & 0 & 0 & 0 \\ -\frac{1}{3}\left(h_a^E + h_b^E - h_c^E\right) & \frac{2}{3}h_b^E & -\frac{1}{3}\left(-h_a^E + h_b^E + h_c^E\right) & 0 & 0 & 0 \\ -\frac{1}{3}\left(h_a^E - h_b^E + h_c^E\right) & -\frac{1}{3}\left(-h_a^E + h_b^E + h_c^E\right) & \frac{2}{3}h_c^E & 0 & 0 & 0 \\ 0 & 0 & 0 & 2h_{ab}^G & 0 & 0 \\ 0 & 0 & 0 & 0 & 2h_{ac}^G & 0 \\ 0 & 0 & 0 & 0 & 0 & 2h_{bc}^G \end{bmatrix} \tag{43}$$

where h_a^E, h_b^E and h_c^E are normal stress hardening parameters in each orthotropic direction and h_{ab}^G, h_{ac}^G and h_{bc}^G are shear stress hardening parameters in each plane. In case there is no preferred direction for kinematic hardening, this tensor may be replaced by the deviatoric projection tensor or by the identity tensor. Note that Eq. (43) guarantees the deviatoric feature of a backstress tensor. We assume that the

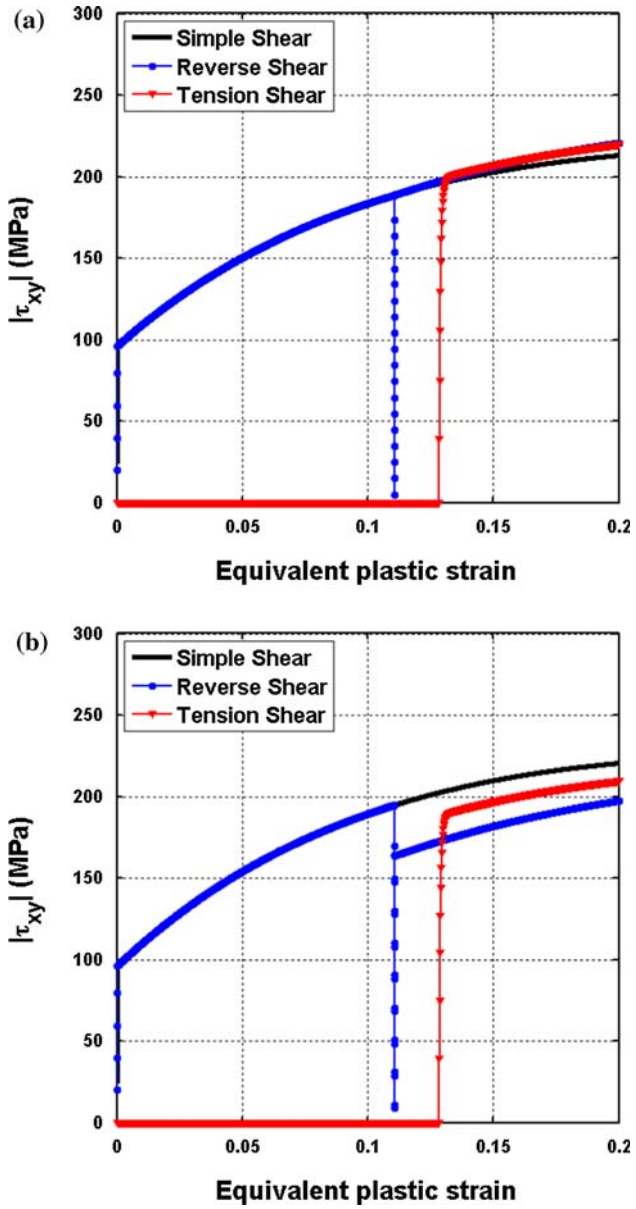

Fig. 14 Multi-path loading response *(without plastic spin)*; **a** isotropic hardening model—neither 'cross' nor 'Bauschinger' effect, **b** mixed hardening model—no 'cross' but 'Bauschinger' effect. ($M = 0.9$, $\mathbb{H} = \mathbb{D}$ where $\mathbb{D}$ is the fourth order deviatoric projection tensor)

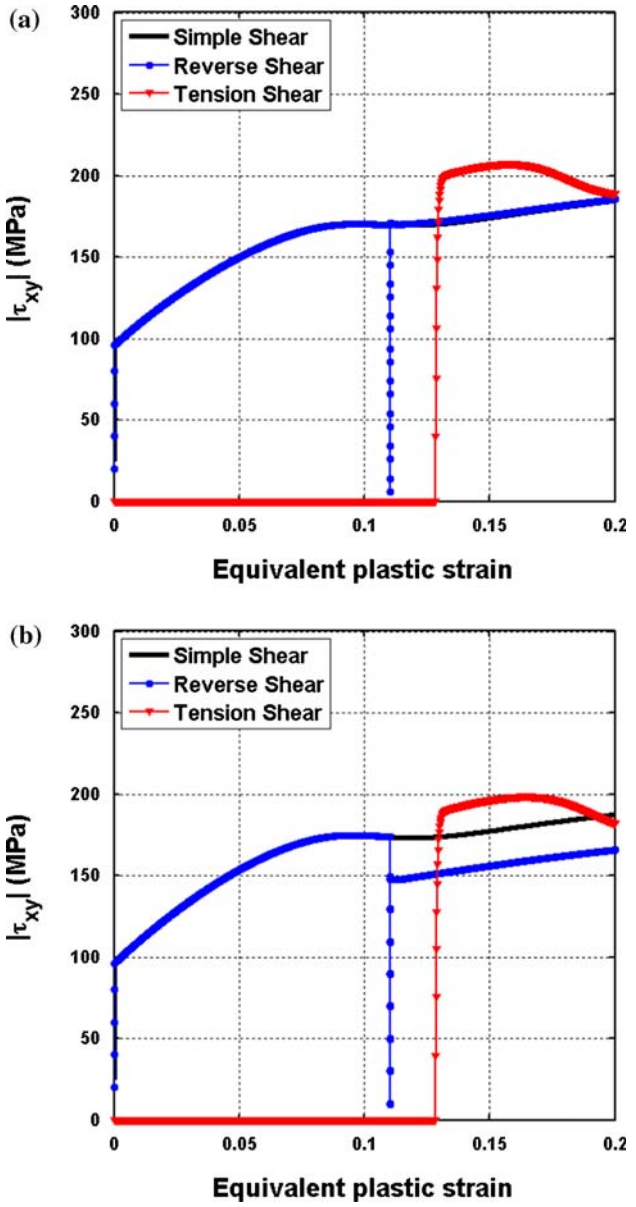

Fig. 15 Multi-path loading response *(with plastic spin)*; **a** isotropic hardening model—'cross' but no 'Bauschinger' effect, **b** mixed hardening model—'cross' and 'Bauschinger' effect. ($M = 0.9, \mathbb{H} = \mathbb{D}$ where $\mathbb{D}$ is the fourth order deviatoric projection tensor)

orthotropic axes for hardening are aligned with those for the elastic tensor and the yield surface.

The same material properties are used as in [44]. The properties are those of two DDQ (deep drawing quality) and one DQ (drawing quality) mild steels. We calibrate the spin parameters and kinematic hardening parameters of our model to fit the experimental results while we adopt the values for isotropic hardening and initial R-values used in [44]. Only small anisotropy is introduced in the elastic constants. The material properties and parameters used in this study are listed in Table 2. Figures 10, 11 and 12 show the results obtained. The predictions show a good agreement with experimental results both in the R-values and the flow stresses for all three materials, which is also achieved by Choi et al. Hence it may be concluded that this method can be an alternative way of identifying parameters for anisotropic axes rotation.

However, much more comparison of computed responses with experimental data on various materials is needed to validate this identification procedure. It would be ideal if we could compare the spin parameters, for the same material, calibrated from the evolution of anisotropies in yield stress

Table 3 The material parameters used in Sect. 5

Elastic constants	R-values	Hardening	Spin
$E_a = 207\,\text{GPa}$	$R_0 = 2.64$	$\kappa_0 = 152.00\,\text{MPa}$	$\rho = 0.40$
$E_b = 206\,\text{GPa}$	$R_{45} = 1.57$	$\kappa_\infty = 387.81\,\text{MPa}$	$\eta = 80$
$E_c = 206\,\text{GPa}$	$R_{90} = 2.17$	$\delta = 9.23, \bar{h} = 0.0$	$m = 1.0$
$\nu_{ab} = \nu_{ac} = \nu_{bc} = 0.3$			
$G_{ab} = 80\,\text{GPa}$			
$G_{ac} = G_{bc} = 79.23\,\text{GPa}$			

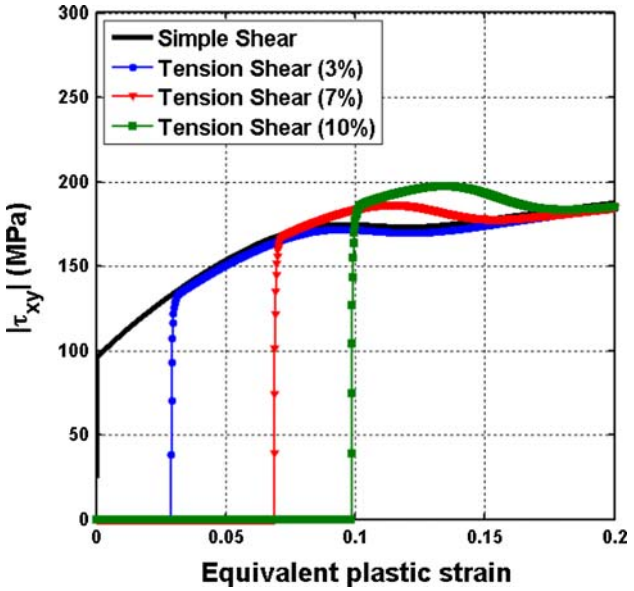

Fig. 16 The effect of the amount of prestraining on crossing. (Isotropic hardening, $M = 1.0$)

as in [32] and from the evolution of the R-values and the flow stresses as in [44].

5 Predictability of the model in multi-paths loading problems

We consider in this section, the capability of our model to predict the behavior in problems where the loading path changes during the plastic deformation. Two key features that we want to capture in multi-paths loading problems are the well-known 'Bauschinger' effect and the 'cross' effect, that is, the effect of uniaxial prestraining on the shear response [45,52]. Three deformation patterns are simulated in order to identify basic features of a multi-paths loading problem as in [45]. The first one is a monotonic simple shear. The second one is a reverse simple shear, where the material is pushed back to its initial shape after a forward shear. The third one is a tension-shear path, where uniaxial prestraining is applied prior to the simple shear. The Bauschinger effect can be seen in the reverse shear test and the cross effect may appear in certain tension-shear tests depending on the materials used. The loading paths are illustrated in Fig. 13.

As reported in [45], the cross effect cannot be captured by a conventional phenomenological model which considers only isotropic and kinematic hardening while, of course, the Bauschinger effect can be modeled with kinematic hardening by the backstress evolution. If the rotation of anisotropic axes is taken into account, the cross effect appears in the predicted response. The calculated responses are shown in Figs. 14 and 15. The material parameters used are listed in Table 3. Note that the amount of crossing depends on how much the material is prestrained prior to the shear deformation. A larger amount of prestraining leads to a greater crossing effect as shown in Fig. 16. It is also interesting that the cross effect is greatly influenced by the amount of kinematic hardening, see Fig. 17. The cross effect becomes prominent as M approaches 1 (purely isotropic hardening). As the portion of kinematic hardening increases (M approaches 0), the cross effect gradually weakens and eventually no crossing takes place after a certain amount of hardening. In that case, the shear stress of a tension-shear test follows a monotonic simple shear curve with an offset.

6 Concluding remarks

Despite the significant advances in the simulations of elasto-plastic responses, the efficient and accurate analysis of large strain deformations of anisotropic sheet metals remains elusive. This is due to the difficulties imposed by the elastic and plastic anisotropy and the evolution thereof.

In this paper, we performed some studies on a model suitable for the analysis of orthotropic elasto-plastic continua considering both the elastic and plastic anisotropy and the evolution of the material symmetries. Elastic anisotropy is a crucial ingredient in the model to capture the rotation of the anisotropy axes. These studies give some physical insight into the model, notably regarding the understanding of the material parameters that affect the evolution of the directions of orthotropy, their effect on the predictions achieved with the model, and hence the proper choice of these parameters. We obtain the material parameters from measurements of elastic and plastic anisotropies including from the evolution of the Lankford coefficients, and find that modeling the elastic anisotropy explains earlier published results.

An effective material model requires the use of a consistent theory, as given in this paper, and a full validation of the model. For our model, a full validation will require the availability of more experimental data and comparisons with simulations. However, the required experimental data is still scarce, especially when including the measurement of elastic anisotropy. It will be very valuable to continue with the validation of the model as more experimental data becomes available.

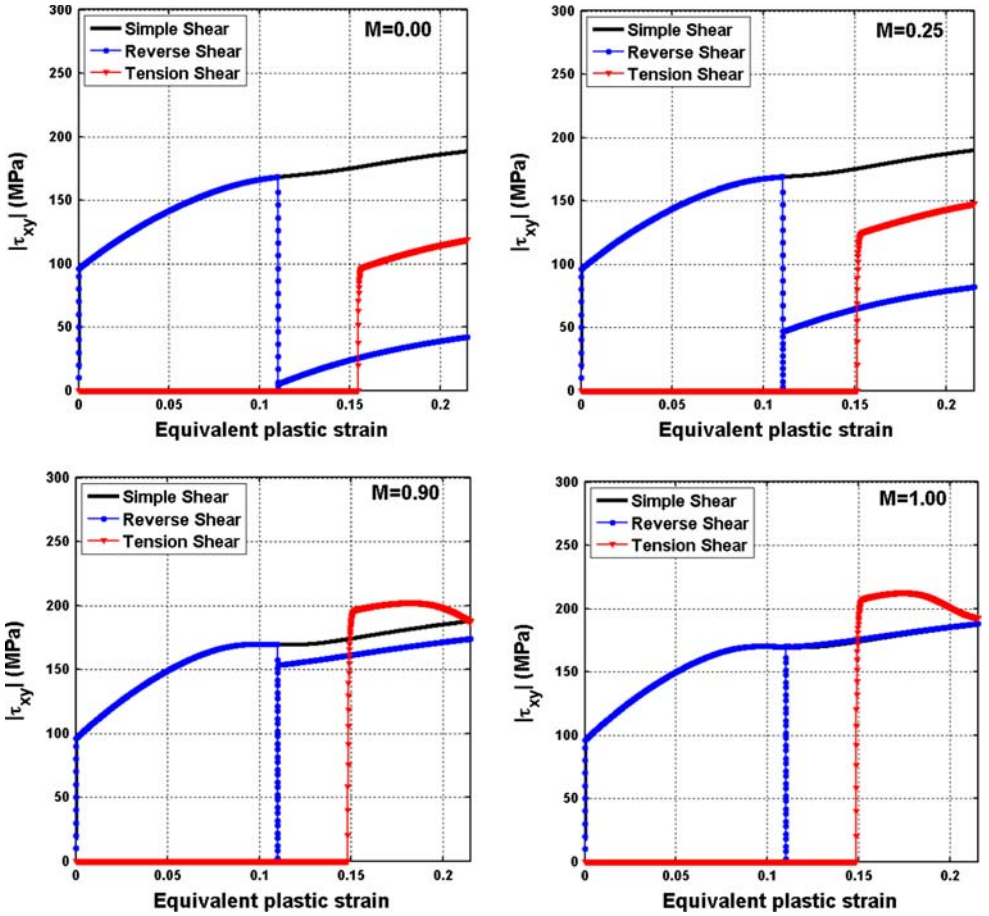

Fig. 17 An effect of the mixed hardening parameter (M) on the cross effect. ($h_a^E = h_b^E = 1.2, h_c^E = 0.6, h_{ab}^G = h_{ac}^G = h_{bc}^G = 0.5$)

Acknowledgments The first author would like to acknowledge the partial support by the Korea Science and Engineering Foundation Grant (No. D00070). The second author is supported by grant DPI2008-05423 of the Ministerio de Ciencia e Innovación of Spain.

References

1. Bathe KJ (1996) Finite element procedures. Prentice-Hall, New Jersey
2. Bathe KJ (2009) The finite element method. In: Wah B (ed) Encyclopedia of computer science and engineering. Wiley, London, pp 1253–1264
3. Kojić M, Bathe KJ (2005) Inelastic analysis of solids and structures. Springer, Berlin
4. Bathe KJ, Montáns FJ (2004) On modeling mixed hardening in computational plasticity. Comp Struct 82:535–539
5. Eterović AL, Bathe KJ (1990) A hyperelastic-based large strain elasto-plastic constitutive formulation with combined isotropic-kinematic hardening using logarithmic stress and strain measures. Int J Num Meth Eng 30:1099–1115
6. Montáns FJ, Bathe KJ (2005) Computational issues in large strain elastoplasticity: an algorithm for mixed hardening and plastic spin. Int J Num Meth Eng 63:159–196
7. Lee EH (1967) Elastic-plastic deformations at finite strains. J Appl Mech 36:1–6
8. Weber G, Anand L (1990) Finite deformation constitutive equations and a time integration procedure for isotropic hyperelastic-viscoelastic solids. Comp Meth Appl Mech Eng 79:173–202
9. Montáns FJ, Bathe KJ (2007) Towards a model for large strain anisotropic elasto-plasticity. In: Oñate E, Owen R (eds) Computational plasticity. Springer, Berlin, pp 13–36
10. Bathe KJ, Ramm E, Wilson EL (1975) Finite element formulations for large deformation dynamic analysis. Int J Num Meth Eng 9:353–386
11. Snyder MD, Bathe KJ (1981) A solution procedure for thermo-elastic-plastic and creep problems. J Nucl Eng Des 64:49–80
12. Simó JC, Ortiz M (1985) A unified approach to finite deformation elastoplasticity based on the use of hyperelastic constitutive equations. Comp Meth Appl Mech Eng 49:221–245
13. Simó JC, Hughes TJR (1998) Computational inelasticity. Springer, New York
14. Kojić M, Bathe KJ (1987) Studies of finite element procedures—Stress solution of a closed elastic strain path with stretching and shearing using the updated Lagrangian Jaumann formulation. Comp Struct 26:175–179
15. Gabriel G, Bathe KJ (1995) Some computational issues in large strain elasto-plastic analysis. Comp Struct 56:249–267
16. Anand L (1979) On H. Hencky's approximate strain-energy function for moderate deformations. J Appl Mech ASME 46:78–82
17. Anand L (1986) Moderate deformations in extension-torsion of incompressible isotropic elastic materials. J Mech Phys Solids 34:293–304

18. Papadopoulus P, Lu J (1998) A general framework for the numerical solution of problems in finite elasto-plasticity. Comp Meth Appl Mech Eng 159:1–18
19. Miehe C, Apel N, Lambrecht M (2002) Anisotropic additive plasticity in the logarithmic strain space: modular kinematic formulation and implementation based on incremental minimization principles for standard materials. Comp Meth Appl Mech Eng 191:5383–5425
20. Eidel B, Gruttmann F (2003) On the theory and numerics of orthotropic elastoplasticity at finite plastic strains. In: Bathe KJ (ed) Computational fluid and solid mechanics. Elsevier, Oxford, pp 246–248
21. Han CS, Choi Y, Lee JK, Wagoner RH (2002) A FE formulation for elasto-plastic materials with planar anisotropic yield functions and plastic spin. Int J Solids Struct 39:5123–5141
22. Han CS, Chung K, Wagoner RH, Oh SI (2003) A multiplicative finite elasto-plastic formulation with anisotropic yield functions. Int J Plast 19:197–211
23. Menzel A, Steinmann P (2003) On the spatial formulation of anisotropic multiplicative elasto-plasticity. Comp Meth Appl Mech Eng 192:3431–3470
24. Haupt P, Kersten Th (2003) On the modeling of anisotropic material behavior in viscoplasticity. Int J Plast 19:1885–1915
25. Itskov M, Aksel N (2004) A constitutive model for orthotropic elasto-plasticity at large strains. Arch Appl Mech 74:75–91
26. Sansour C, Karsaj I, Soric J (2007) On anisotropic flow rules in multiplicative elastoplasticity at finite strains. Comp Meth Appl Mech Eng 196:1294–1309
27. Schmidt I (2005) Some comments on formulations of anisotropic plasticity. Comp Mater Sci 32:518–523
28. Kowalewski ZL, Sliwowski M (1997) Effect of cyclic loading on the yield surface evolution of 18G2A low-alloy steel. Int J Mech Sci 39:51–68
29. Bunge HJ, Nielsen I (1997) Experimental determination of plastic spin in polycrystalline materials. Int J Plast 13:435–446
30. Truong Qui HK, Lippmann H (2001) Plastic spin and evolution of an anisotropic yield condition. Int J Mech Sci 43:1969–1983
31. Boheler JP, Koss S (1991) Evolution of anisotropy in sheet steels subjected to off-axes large deformation. In: Brüller O, Mannl V, Najar J (eds) Advances in continuum mechanics. Springer, Berlin, pp 143–158
32. Kim KH, Yin JJ (1997) Evolution of anisotropy under plane stress. J Mech Phys Solids 45:841–851
33. Bunge HJ (1982) Texture analysis in materials science. Butterworths, London
34. Kocks U, Tomé C, Wenk H (1998) Texture and anisotropy. Cambridge University Press, New York
35. Wu PD, Neale KW, Van der Giessen E (1996) Simulation of the behaviour of FCC polycrystals during reversed torsion. Int J Plast 12:1199–1219
36. Peeters B, Hoferlin E, Van Houtte P, Aernouldt E (2001) Assessment of crystal plasticity based calculation of the lattice spin of polycrystalline metals for FE implementation. Int J Plast 17: 819–836
37. Van Houtte P, Li S, Seefeldt M, Delannay L (2005) Deformation texture prediction: from Taylor model to the advanced Lamel model. Int J Plast 21:589–624
38. Buchheit TE, Wellman GW, Battaile CC (2005) Investigating the limits of polycrystal plasticity modeling. Int J Plast 21:221–249
39. Nakamachi E, Tam NN, Morimoto H (2007) Multiscale finite element analysis of sheet metals by using SEM-EBSD measured crystallographic RVE models. Int J Plast 23:450–489
40. Duchene L, Houdaigui F, Habraken AM (2007) Length changes and texture prediction during free end torsion test of copper bars with FEM and remeshing techniques. Int J Plast 23:1417–1438
41. Raabe D, Roters F (2004) Using texture components in crystal plasticity finite element simulations. Int J Plast 20:339–361
42. Raabe D, Wang Y, Roters F (2005) Crystal plasticity simulation study on the influence of texture on earing in steel. Comp Mater Sci 34:221–234
43. Delaire F, Raphanel JL, Rey C (2000) Plastic heterogeneities of a copper multicrystal deformed in uniaxial tension: Experimental study and finite element simulations. Acta Mater 48:1075–1087
44. Choi Y, Walter ME, Lee JK, Han C-S (2006) Observations of anisotropy evolution and identification of plastic spin parameters by uniaxial tensile tests. J Mech Mat Struct 1:303–324
45. Choi Y, Han C-S, Lee JK, Wagoner RH (2006) Modeling multiaxial deformation of planar anisotropic elasto-plastic materials, part I: Theory. Int J Plast 22:1745–1764
46. Dafalias YF (1985) The plastic spin. J Appl Mech ASME 52:865–871
47. Dafalias YF, Aifantis EC (1990) On the microscopic origin of the plastic spin. Acta Mech 82:31–48
48. Dafalias YF (1998) The plastic spin: necessity or redundancy? Int J Plast 14:909–931
49. Dafalias YF (2000) Orientational evolution of plastic orthotropy in sheet metals. J Mech Phys Solids 48:2231–2255
50. Loret B (1983) On the effects of plastic rotation in the finite deformation of anisotropic elastoplastic materials. Mech Mater 2:287–304
51. Tvergaard V (2001) Plastic spin associated with non-normality theory of plasticity. Eur J Mech A/Solids 20:893–905
52. Peeters B, Seefeldt M, Teodosiu C, Kalidindi SR, Van Houtte P, Aernoudt E (2001) Work-hardening/softening behavior of B.C.C. polycrystals during changing strain paths: I. An integrated model based on substructure and texture evolution, and its prediction of the stress-strain behavior of an IF steel during two-stage strain paths. Acta Mater 49:1607–1619